Investigation of Resistance Switching in SiO_x RRAM Cells Using a 3D Multi-Scale Kinetic Monte Carlo Simulator

Toufik Sadi[1,2*], Adnan Mehonic[3], Luca Montesi[3], Mark Buckwell[3], Anthony Kenyon[3], and Asen Asenov[1]

[1]School of Engineering, Electronic and Nanoscale Engineering, University of Glasgow, Glasgow G12 8LT, Scotland, UK

[2]Department of Neuroscience and Biomedical Engineering, Aalto University, P.O. Box 12200, FI-00076 AALTO, Finland

[3]Department of Electronic and Electrical Engineering, University College London, London WC1E 7JE, UK

*Email: Toufik.Sadi@aalto.fi

Abstract

We employ an advanced three-dimensional (3D) electro-thermal simulator to explore the physics and potential of oxide-based resistive random-access memory (RRAM) cells. The physical simulation model has been developed recently, and couples a kinetic Monte Carlo study of electron and ionic transport to the self-heating phenomenon while accounting carefully for the physics of vacancy generation and recombination, and trapping mechanisms. The simulation framework successfully captures resistance switching, including the electroforming, set and reset processes, by modeling the dynamics of conductive filaments in the 3D space. This work focuses on the promising yet less studied RRAM structures based on silicon-rich silica (SiO_x) RRAMs. We explain the intrinsic nature of resistance switching of the SiO_x layer, analyze the effect of self-heating on device performance, highlight the role of the initial vacancy distributions acting as precursors for switching, and also stress the importance of using 3D physics-based models to capture accurately the switching processes. The simulation work is backed by experimental studies. The simulator is useful for improving our understanding of the little-known physics of SiO_x resistive memory devices, as well as other oxide-based RRAM systems (e.g. transition metal oxide RRAMs), offering design and optimization capabilities with regard to the reliability and variability of memory cells.

1. INTRODUCTION

Resistive random-access memories (RRAMs) are promising nonvolatile memory based devices. They have attracted considerable attention in the last 10 years [1]–[15]. The 2010 International Technology Roadmap for Semiconductors (ITRS) report on emerging devices details the incentives for developing RRAM device technologies, namely reduced power dissipation and cost-per-bit, increased endurance, and suitability for chip incorporation as 3D crossbar arrangements. RRAMs are suitable for a multitude of technological applications, including neuromorphic computing [16] and neural networks [17], [18].

RRAMs are often linked with the concept of memristors. The concept of a memristor was suggested in the 1970's [19], but it was only in 2008 that one of the first links between the theoretical framework and experiments was demonstrated, by using e.g. titanium dioxide (TiO_2) [13]. Several RRAM technologies are nowadays under investigation. In this context, oxide-based RRAMs represent one of the most studied devices; materials of interest include metal oxides [13], such as TiO*x* and HfO*x*, and SiO*x* [1], [20], [21]. There is also a huge interest in RRAMs based on phase-change materials, such as perovskite materials, Ge sulphide and selenide, and chalcogenides [10], [22], [23]. Particularly, chalcogenide-based RRAMs [22], [23] show a great potential in applications based on the Programmable Metallization Cell (PMC) technology platform. Moreover, there is an increasing interest in less known memristor structures, e.g. the ferroelectric memristor [7] whose operation is entirely due to electron dynamics. Transition metal oxides (TMOs) are generally characterized by a high dielectric constant, which is a highly desirable feature towards high-density electronic integration. While RRAMs based on TMOs are nowadays considered as the most promising technology, they face many significant challenges, most notably Si microelectronics integration. On the other hand, the development of RRAM devices based on silicon-rich silica – SiO*x* ($x < 2$) – as studied in this article, can potentially result in cheap integration in silicon CMOS chips.

This article is organized as follows. In Section 2, we discuss the current progress in RRAM device modelling and the main features of our simulator. In Section 3, we present a detailed description of the simulation framework. In section 4, we show results from the application of the simulator to TiN/SiO*x*/TiN RRAM structures. The results are analyzed and their significance is discussed. In section 5, we draw conclusions about the main results and the simulation work is general.

2. RRAM SIMULATION: STATE-OF-THE-ART AND BEYOND

Resistance switching in oxide RRAMs occurs via the electro-formation and rupture of a conductive filament (CF) [24], as oxygen vacancies are created and ions are redistributed in the oxide under the influence of the local electric field and temperature. Most work on RRAMs focuses on devices based on TMOs, as highlighted above. Moreover, previous RRAM simulation studies relied heavily on phenomenological modeling techniques (e.g. the resistor breaker network method) [14], [25] and two-dimensional approaches [9], [26]. These models do not determine in a self-consistent manner the electric fields and do not consider accurately the physics of device self-heating (heat generation and conduction).

The drive to develop reliable simulation models for RRAMs is still strong, as illustrated by the continued increase in the number of publications on this topic (please see e.g. Refs. [25], [27]–[30]). There is an interest in both developing advanced models – of analytical (e.g. Ref. [30]), circuit-based (e.g. Ref. [25]) and multi-physical (e.g. Ref. [27]–[29]) nature – and studying specific

effects such as the crosstalk effect [27]. Continuous efforts are also made to understand further the physics of SiO*x* RRAM structures [31].

We utilize a recently developed three-dimensional (3D) kinetic Monte Carlo (KMC) simulator to investigate the behavior of SiO_x RRAM memory cells. The novel aspects of our work lie in the advanced features of our simulator as well as in the focus on the less-studied but highly-interesting SiO*x* RRAM devices. Our modeling approach has unique capabilities that distinguish it from previously presented models [9], [14], [26]. Firstly, the simulator employs a powerful framework, considering electron-ion interactions to reconstruct realistically the electroforming and rupture of the CF in the 3D real space. Secondly, it couples in a self-consistent fashion time-dependent electron and oxygen ion transport (stochastic KMC) simulations to the local temperature and electric field 3D distributions, determined by solving the relevant physical equations. Thirdly, the simulator accounts accurately for the dynamic nature of the ion-vacancy generation process in SiO*x*, as detailed in [32]. Fourthly, the simulator accounts carefully for trapping dynamics and electron transport mechanisms in the oxide [33], [34]. Fifthly, the simulation work is supported by experimental studies by the authors demonstrating switching in SiO*x* RRAMs at room temperature (see e.g. Refs. [1], [35]).

3. SIMULATION METHODOLOGY

We study the SiO*x*-based structure shown in Fig. 1 [35]. The structure consists of a SiO*x* layer of thickness H=10nm sandwiched between two titanium nitride (TiN) contacts. The TiN plates in typical experimental devices have an area of 100μm×100μm [1]. In this study, we can limit this simulation study to a much smaller area (e.g. L×W=20nm×20nm), corresponding to a region containing e.g. a grain boundary. Indeed, experiments by the authors suggest the existence of only one dominating conductive filament per plate [1], in typical structures. The simulation framework involves the rigorous time-dependent coupling of electron and oxygen ion dynamics to the local temperature and electric field in the oxide volume. The flowchart shown in Fig. 2 illustrates the simulation procedure. Figure 3 illustrates the mechanisms governing electron transport in the oxide. The simulator is supported by experimental results obtained from SiO*x* RRAM devices [1], [35], as discussed before. The simulator employs a structure generation editor, which allows the building of a device structure of any arbitrary geometrical features and material composition.

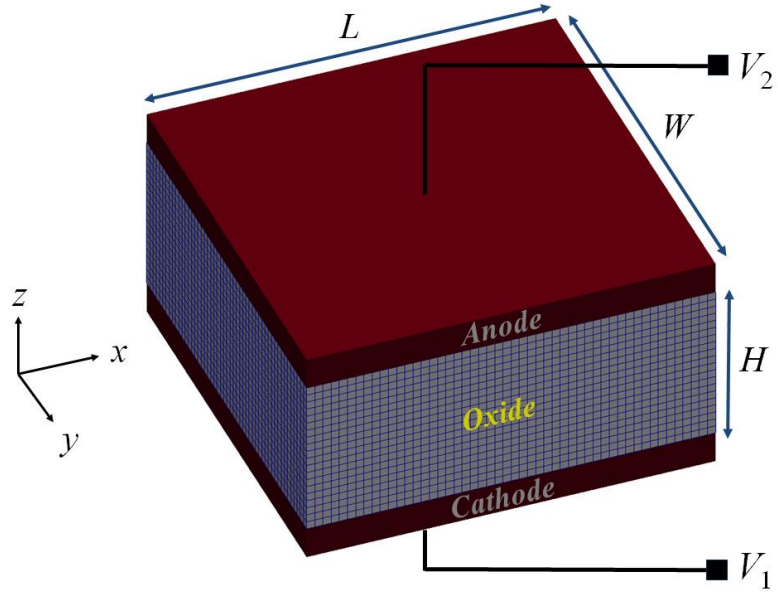

Fig. 1. The simulated SiO*x* RRAM structure, with an oxide layer of thickness *H*=10nm sandwiched between two TiN contacts. While experimental devices have large areas (~100μm×100μm) [1], we can limit the simulations to a much smaller (Si-rich) area (e.g. *L*×*W*=20nm×20nm), where a grain boundary may be present.

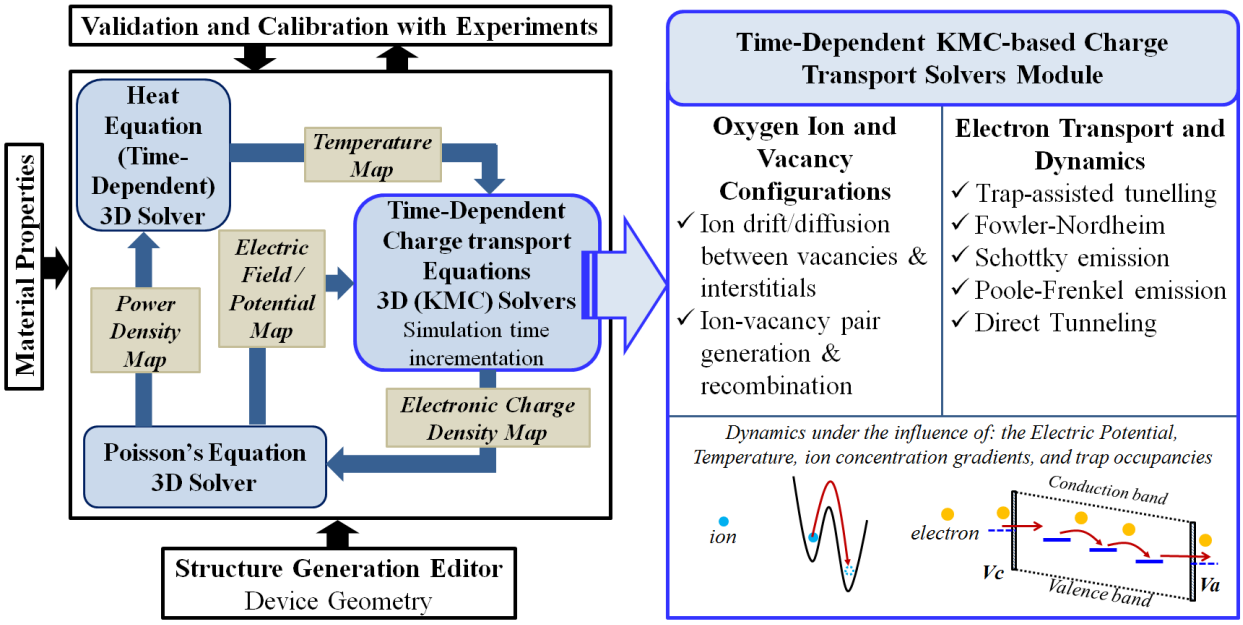

Fig. 2. The full simulation procedure, which involves the coupling of a KMC description of the electron and oxygen ion transport phenomena to the temperature and electric field distributions in the oxide volume, in a self-consistent manner. The simulator accounts carefully for the vacancy generation process.

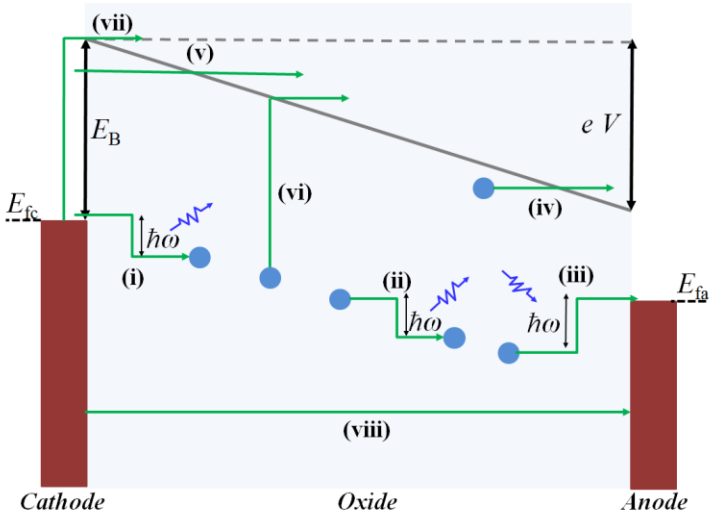

Fig. 3. The processes governing electron transport, as implemented in the simulator. They include trap-assisted tunneling processes [i.e. (i) electrode-trap, (ii) trap-trap, (iii) trap-electrode, and (iv) electron to the conduction band (CB) tunneling mechanisms], (v) Fowler-Nordheim tunneling mechanism, (vi) Poole-Frenkel emission (of an electron from a given trap to the CB), (vii) Schottky emission, and (viii) direct electron tunneling (from one contact terminal to another).

3.1. Ion and Vacancy Dynamics

The simulator allows the accurate study of resistance switching resulting from the electroformation and rupture of CFs. We us a stochastic kinetic Monte Carlo description to model the drifting and diffusion of ions between interstitial sites and oxygen vacancies, and ion-vacancy pair generation and recombination processes. The simulator solves for the oxygen ion transport equation given by:

$$\nabla \bullet \left[D\nabla n_I(\vec{r},t) - V_I n_I(\vec{r},t) \right] + R_G = \frac{\partial n_I(\vec{r},t)}{\partial t}, \tag{1}$$

where n_I and V_I are the ion concentration and velocity, D is the diffusivity coefficient, and R_G is the net rate of ionic generation. $\vec{r}$ and t represent spatial position and time. The inclusion of vacancy dynamics is not important in the studied devices, considering the fact that the diffusion barrier of the vacancies is relatively high (4eV as compared to 0.3eV for ions). As the field and temperature distributions are updated regularly, relevant physical quantities are re-calculated, including the attempt-to-escape rate for oxygen to jump over the barrier P_g (ion-vacancy generation rate), and the probability of ion-vacancy recombination P_r:

$$P_g = f_0 \exp\left[-\frac{(E_a - \gamma eE)}{k_b T} \right], \tag{2}$$

$$P_r = C_{ion} f_0 \exp\left[-\frac{(E_r - \gamma eE)}{k_b T} \right], \tag{3}$$

where E_a is the formation energy, E_r is the recombination barrier, γ is the contribution of the bond polarization to the local electric field **E** (with magnitude E), C_{ion} is the ion concentration, T is the lattice temperature, k_b is the Boltzmann constant, and e is the electronic charge. The generated ions move through lattice sites (including interstitials and vacancies), either by drifting with an average

velocity V_I (field and temperature-assisted ion hopping), or diffusing according to the related diffusion constant D. Ions drift or diffuse according to probabilities P_{dr} and P_{df} given by:

$$P_{dr} = f_0 \exp\left(-\frac{(E_m - eaE)}{k_b T}\right), \tag{4}$$

$$P_{df} = \frac{1}{2} f_0 \exp\left(-\frac{E_m}{k_b T}\right), \tag{5}$$

leading to average velocities and diffusion constants given by:

$$V_{ion} = a f_0 \exp\left(-\frac{E_m}{k_b T}\right) \sinh\left(\frac{eaE}{2k_b T}\right), \tag{6}$$

and

$$D = 1/2 a^2 f_0 \exp\left(-\frac{E_m}{k_b T}\right), \tag{7}$$

where a is the lattice constant and E_m is the oxygen migration barrier. The values of relevant parameters are summarized in Table 1, which are collected from selected publications including [36] and [37].

For the reliable modelling of switching in SiO_x RRAM devices, the process of vacancy generation through bond breakage needs to be carefully accounted for. Extensive data related to bond breakage and breakdown in silica has been collected, as reported in Ref. [36]. Two sets of values have been suggested for the activation energy (E_a) and the 'contribution of the bond polarization to the local electric field' parameter (γ): (i) E_a=1eV and γ=7eÅ, and (ii) E_a=2eV and γ=13eÅ. Both data sets (i) and (ii) give a breakdown field of ~15 MV/cm. We use the vacancy generation model reported by the authors in Ref. [32]. In this model, a generation event produces an oxygen vacancy and a negatively charged oxygen interstitial ion O^{2-}. The generated ion moves rapidly through the oxide layer (with a migration barrier of around 0.3eV), as discussed in previous experimental work [37]. While the normal generation process data are used in SiO_2 (E_a=1eV and γ=7eÅ), Ref. [32] describes how neutral oxygen vacancies occupied by two electrons result in lowering E_a (<1eV ; ~0.7eV) and enhancing the generation rate in defect-rich areas. The recombination process is assumed to be the exact reverse process of the generation mechanism with a recombination rate $P_r = C_{ion} P_g$, where C_{ion} is the relative concentration indicating the presence (C_{ion} =1) or absence (C_{ion} =0) of an ion at a vacancy site. As is the standard practice (see e.g. Ref. [38]), recombination only occurs if the vacancy (positive or neutral) is depleted of electrons to satisfy charge conservation.

Table 1. The main parameters used in the simulations, which are collected from selected publications including [36] and [37].

Parameter	Value
f_0: vibration frequency	10^{13} s^{-1}
E_a: formation energy	1eV
E_r: recombination barrier	1eV
E_m: Oxygen migration barrier	0.3eV
a: Lattice constant	5Å
γ: contribution of the bond polarization to the local electric field	7eÅ

3.2. Electron Transport

The processes governing electron transport in oxide-based RRAM devices, as considered in this work, are summarized in Fig. 3. These include the trap-assisted tunneling (TAT) processes (i.e. electrode-trap, trap-trap, trap-electrode, and trapped electron to the conduction band (CB) tunneling mechanisms), the Fowler-Nordheim tunneling mechanism, Poole-Frenkel emission (of an electron from a given trap to the CB), Schottky emission, and direct electron tunneling (from one contact terminal to another) [33]. Careful consideration of TAT tunneling is especially necessary for the accurate updating of the occupancy of the traps. In this work, we apply a KMC algorithm to track down the trapped electron population in the oxide and update the occupancy of traps, instead of using the simpler current solver described in Ref. [9]. Below is a discussion of the dominating transport mechanisms, including trap-assisted tunneling. Other mechanisms are thoroughly discussed in literature (see e.g. Ref. [33]).

1) Trap-trap tunneling: This is an important mechanism for electric conduction in relatively thick oxide layers, as considered here (see e.g. Ref. [33] for more information). Consider two trap states located at a distance R apart, with energies E_1 and E_2. In the case "$W= E_1–E_2> 0$", an electron hops from vacancy (1) to vacancy (2) by the emission of phonons with a total energy $W=p\hbar\omega$, with a hopping rate $R_{1–2}$:

$$R_{1-2} = f_0 \exp\left(-\frac{2R}{\xi}\right) f_1 (1 - f_2), \tag{8}$$

where f_0 is the vibration frequency, ξ is the localization length, f_1 and f_2 are the trap occupancies for the left and right traps respectively, and $\hbar$ is the reduced Planck's constant. Hopping from trap (2) to trap (1) is accompanied by the absorption of phonons (a total energy $W=p\hbar\omega$), with a rate $R_{2–1}$:

$$R_{2-1} = f_0 \exp\left(-\frac{2R}{\xi}\right) f_2 (1 - f_1) \exp(-W/k_bT) \tag{9}$$

2) Electrode-trap tunneling: Electric current flow through the contacts occurs mainly via two mechanisms, as illustrated in Fig. 3: electrode-trap (ET) and trap-electrode (TE) tunneling. The tunneling from an electrode into a trap and the reverse process of emission of trapped electrons

into the electrode are described as a multi-phonon assisted tunneling process. The tunneling rates (to or from trap position z_T) are given by:

$$R_{ET}(E_e) = N(E_e)F(E_e)T_{ET}(E_e)c_{ET}(E_e, z_T), \tag{10}$$

and

$$R_{TE}(E_e) = N(E_e)[1 - F(E_e)]T_{ET}(E_e)c_{ET}(E_e, z_t), \tag{11}$$

where E_e is the tunneling electron energy, N is the density of states in the electrode, F is the Fermi-Dirac distribution function, T_{ET} and T_{TE} are the transmission coefficients, and c_{ET} and c_{TE} denote the corresponding electron-phonon scattering rates, as detailed in Ref. [33]. In this work, T_{ET} and T_{TE} are calculated using the Wentzel-Kramers-Brillouin (WKB) approximation, as follows:

$$T_{ET}(E_e) = \exp\left(-\tfrac{2}{\hbar}\int_{z_E}^{z_T}\sqrt{2m^*(E_C - E_e)}dz\right), \tag{12}$$

$$T_{TE}(E_e) = \exp\left(-\tfrac{2}{\hbar}\int_{z_T}^{z_E}\sqrt{2m^*(E_C - E_e)}dz\right), \tag{13}$$

where z_E is the electrode position, m^* is the effective oxide mass (~$0.42m_0$ for SiO_2), and E_C is the conduction band.

3) Trap levels: To model accurately electron transport via trap-assisted tunneling, we need to employ reliable energy levels for the different traps that are presented in the oxide. The types and details of the traps contributing to trap-assisted tunneling in SiO*x* are described in Ref. [34]. In principle, any trap type (positively charged, neutral or negatively charged) can contribute to trap-to-trap hopping and other TAT mechanisms. Albeit, the rate can vary significantly with trap energy levels. Considering the thermal ionization energies E_T for each trap type (5eV for a positive vacancy, and 3.37eV for a neutral vacancy), the neutral oxygen vacancy is the defect assisting the electron TAT in silica, as highlighted in Ref. [34]. This is in contrast to HfO*x*, where positive oxygen vacancies (E_T=1.4–2.4eV) assist the electron TAT mechanisms [34].

4) Other mechanisms: Considering the relatively thick oxide layer (>10nm), the probability of direct tunneling between the two electrodes is extremely low. At high applied biases, direct tunneling merges into the Fowler-Nordheim tunneling. These mechanisms are also modelled within the WKB approximation. As discussed in Ref. [33], these effects are only important when the conduction band offset (CBO) is very small, which is not the case for the TiN/SiO*x*/TiN structure studied here. Poole-Frenkel mechanisms start to visibly contribute to transport if large electric fields are applied [33]. In the simulated devices, Poole-Frenkel events are relatively rare considering the depth of the traps.

3.3. Self-Consistent Fields and Self-Heating

As the positions of charged particles (electrons at traps and oxygen ions) are followed in time (and vacancies are created or destroyed), the local electric potential ϕ is updated in a self-consistent manner using the corresponding local charge densities, by employing an in-house 3D Poisson's equation solver developed by the authors. The simulator is efficiently designed to minimize computational time, which can be high due to the differences (up to few orders of magnitude) in

the time scales between the ionic and electron transport phenomena [39]. The simulation framework uses an adaptive field-adjusting time, allowing accurate self-consistent field coupling with a minimized computational cost. In this scheme, Poisson's equation is only solved when there is an event that leads to a change in the local charge density (e.g. an electron hopping/TAT event or an ion hopping event). The electric field is simply related to the local potential ϕ via the relationship $\vec{E} = -\nabla\phi$. Simultaneously, temperature rise due to self-heating is calculated by the resolution of the time-dependent heat diffusion equation (HDE)

$$\nabla \bullet \left[\kappa(\vec{r},T)\nabla T(\vec{r},t)\right] + g(\vec{r},t) = \rho C \frac{\partial T(\vec{r},t)}{\partial t}, \tag{14}$$

employing an advanced numerical solver. In equation (14), T and g are the temperature and thermal power density (heat generation), respectively, and κ is the thermal conductivity. C and ρ are the specific heat capacity and material density, respectively. The contributions of ion and electron dynamics to heat generation are determined by the dot product of the local field and current density vectors $\vec{J} \bullet \vec{E}$, assuming Joule heating is the dominant mechanism for dissipation. As in the standard practice in time-dependent stochastic (Monte Carlo) simulations, the local current density is also updated regularly, as ions and electrons move and vacancies are created or destroyed in the oxide.

3.4. Kinetic Monte Carlo Algorithm: Motivation and Application

In our previous publication [32], we highlighted the importance of trapping and electron-ion interactions in influencing the vacancy generation processes in SiO*x*. To model such processes, it is important to track down the real occupancy of each trap in time, which can only be achieved using direct solvers based on the stochastic KMC algorithm, not just for ions, but also for electrons. In this case, steady-state models are not best suited for studied SiO*x* RRAM devices.

1) KMC algorithm for ions: The simulator constructs the device geometry by assuming a 3D matrix of SiO_2 molecules and (initial) oxygen vacancies at lattice sites, sandwiched between two contacts where Dirichlet boundary conditions are imposed. Ion-vacancy generation events are selected (in time) according to the probability P_g using random numbers. As ions are generated, they move from one lattice point to another neighbouring lattice point, which can be either a vacancy or an interstitial, or to one of the electrodes. The trajectory of a moving ion is selected using the KMC algorithm, by building cumulative drifting and diffusion probability (P_{dr} and P_{df}) ladders (considering all possible neighboring lattice sites and/or electrodes) and using a random number to choose the subsequent destination of each ion. Similar to the generation process, an ion-vacancy recombination process is selected randomly according to probability P_{r}.

2) KMC algorithm for electrons: Similar to the ion KMC algorithm, we model electron movements according to the hopping and tunneling rates given by equations (8)–(13). For each electron in the oxide layer, we build a cumulative hopping and tunneling rate ladder including all possible destinations (vacancies or electrodes). The final destination is selected from the ladder using a random number. Furthermore, electrons are injected from the electrodes (to occupy a vacancy or tunnel through) using the same cumulative ladder approach, considering rates from equations (10)–(13).

4. RESULTS AND DISCUSSION

First, we discuss how the experimental studies of the SiO_x RRAM devices guide the simulation work. Then, we validate and illustrate the capabilities of our simulator by studying the corresponding structures. Finally, we discuss the importance of 3D KMC modelling and self-heating, and show how the initial concentrations of intrinsic traps can affect resistance switching.

4.1. Experimental Characteristics

Figure 4 demonstrates the operation of SiO_x RRAMs by showing an example of experimental *I*−*V* characteristics, for a typical TiN/SiO_x/TiN structure. The *I*–*V* curve demonstrates a typical unipolar mode of resistance switching. Electroforming and set processes are obtained by sweeping the devices and applying the current compliance to prevent hard breakdown. The reset process occurs in the same polarity at voltages lower than the set voltage, by removing the current compliance and allowing the higher current to pass through the device. Our structures include defect/Si-rich regions, which in general facilitate the creation of CFs, by allowing lower forming/set biases, as compared to pristine structures. Previously (experimentally) studied metal-free poly-Si/SiO_x/Si structures [1] showed similar behavior. Also, many studied experimental devices showed surface oxygen bubbles at the anode related to oxygen emission during operation [35]. The results lead to the conclusion that switching is an intrinsic property of the SiO_x layer, and SiO_x RRAMs do not require the diffusion of metallic ions (which can affect adversely the surrounding devices), and confirm that including the metallic diffusion in our model is not necessary. Also, as compared to pristine SiO_2 structures, the existence of Si-rich regions minimizes the possibility of hard breakdown and hence irreversible ON (low resistance) / OFF (high resistance) state transitions. In Ref. [1], the authors reported a resistance contrast of at least 10^4, for at least 120 hours of RRAM OFF/ON cycling.

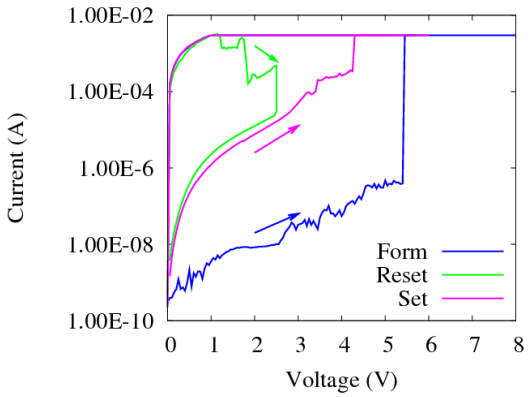

Fig. 4. Experimental *I*−*V* characteristics of a typical SiO_x RRAM structure, for unipolar switching.

4.2. Time-to-Failure Tests

The first step in verifying our KMC simulator model is to reconstruct established data related to time-to-failure (TF) in thin layers, based on pristine silica and (for the sake of comparison) hafnia. For this purpose we employ the vacancy generation parameters described in the work by McPherson *et al.* [36]; the activation energy and field acceleration parameter for SiO_2 (HfO_2) are taken to be 1eV (1.55eV) and 3.5cm/MV (15.4cm/MV), respectively. Figure 5 shows the variation of the TF with the applied electric field, at 300K, as obtained from our simulations (for a 10nm

oxide structure) and published results in Ref. [36]. As can be observed, very good agreement is obtained for both material systems.

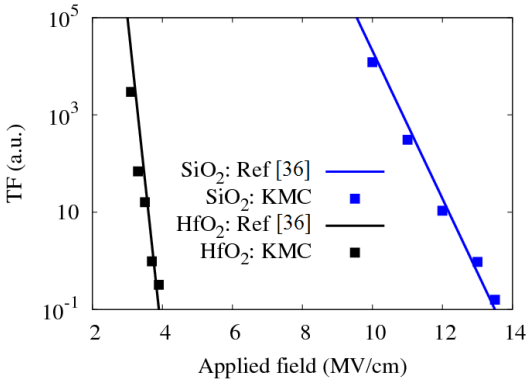

Fig. 5. Time-to-failure using our model, and the data/parameters presented in [36], for both SiO_2 and HfO_2.

4.3. Simulated Characteristics

Figure 6(a) shows the *I*−*V* characteristics (bipolar mode) of an RRAM device with an oxide volume $H \times L \times W$=10nm×50nm×50nm. Figure 6(b) shows the corresponding variation of the peak temperature in the oxide. In the simulations, we use a bias ramping rate of 0.2V/μs. Clearly, the memristive nature of the RRAM *I*−*V* characteristics is correctly captured, distinguishing the three different operating regimes: the electroforming process (where the CF is created), and the subsequent set and reset processes, matching the trends observed in our experiments [1]. As can be seen from Fig. 6(b), the peak temperatures follow a similar trend to the currents. The peak temperature reaches relatively high values (~470K) after the formation of the CF, when the device operates at a low-resistance state (LRS). It is noteworthy that the *I*−*V* characteristics calculated in this paper are from the first cycle after the forming of the conductive filament. Due to the stochastic nature of charge transport in the device, the *I*−*V* characteristics (and hence the resistance of the LRS and high-resistance state (HRS)) vary from one cycle to another [35], [38], and depend significantly on the bias ramping rate, as discussed in Ref. [9]. Also, as discussed in Ref. [40], memristors exhibit a stochastic behavior and that their switching depends strongly on the wait time. The stochastic nature of transport is very well captured by the KMC approach [9]. Fig. 6(c) shows the LRS and HRS resistances for the first 5 cycles, during the set process. While fluctuations are observed in the LRS and HRS resistances, a resistance contrast ratio nearing 10 is maintained at the fifth cycle. The dependence of the *I*−*V* characteristics on the number of testing cycles was illustrated experimentally by the authors in Ref. [35] (for up to 150 cycles); the results show that a contrast ratio of more than a 100 is maintained after 150 cycles, despite the visible fluctuations in the resistance at both the LRS and HRS.

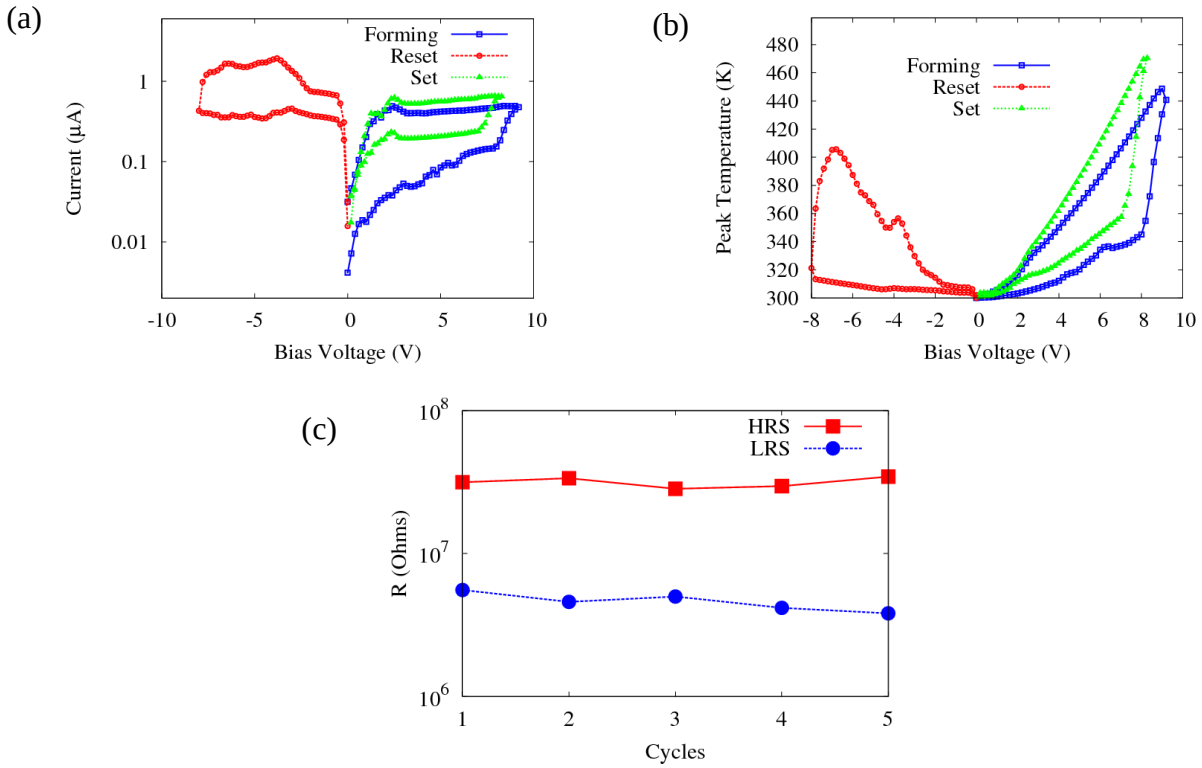

Fig. 6. (a) The *I–V* characteristics, (b) variation of the peak temperature with bias, and (c) the LRS and HRS resistances for 5 cycles (during the set process), for a device with an arbitrary initial oxygen vacancy population. The compliance limit for the current is 10^{-6} A. The bias ramping rate is 0.2V/μs.

To demonstrate heat conduction, we show in Fig. 7 the 3D spatial distribution of temperature in the oxide, at various switching stages: as the CF is created during the electroforming step, ruptured in the reset step, and recreated in the set step. In general, the peak temperature is located in the CF. However, the temperature can still be high outside the CF as heat diffuses to other areas of the device. Indeed, the self-heating phenomenon has a significant effect on transport, particularly during the electroforming process and at the ON state. Despite the relatively low current flow between the two device terminals (and the corresponding low power dissipation), the peak temperature reaches ~450K at the ON state. In this type of structure, device heating (manifested by high operating temperatures) must not be neglected for two different reasons: 1) the elevated values of the current densities through the various percolation paths in the CF, and 2) the relatively low thermal conductivity of SiO*x*.

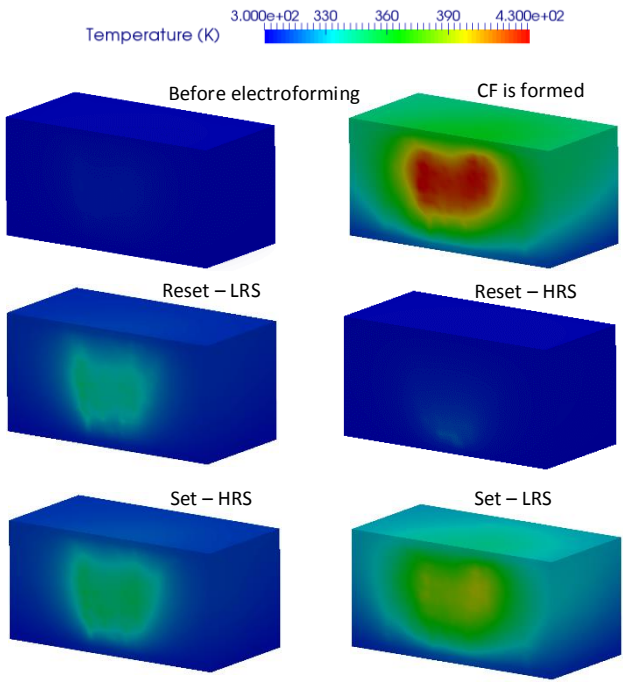

Fig. 7. Example of 3D temperature distributions in the oxide volume, taken to illustrate the heat conduction phenomenon at different switching stages. The results are from a device with an arbitrary initial oxygen vacancy population.

Fig. 8 shows the variation of the local peak temperature with time, illustrating the dynamic nature of heat flow, for different biasing conditions: (i) at a low bias before the forming of the CF, (ii) at a high bias where individual vacancies start to form, and (iii) at around the forming bias where a continuous generation of vacancy-ion pairs occurs leading to the CF creation. Fig. 8 shows very short spikes in temperature, resulting from the ionic currents occurring when vacancy-ion pairs are created, moving relatively quickly to the anode. At a low bias, the temperature is ~300K, as the device current is very low. The peak temperature starts to increase in a modest fashion, as bias is increased and more vacancies (conductive channels) are generated. At a high bias, before the forming of the CF, several vacancy-ion pairs are generated but the overall temperature stays low, as no fully-formed conductive paths are present between the two electrodes. At around the forming bias and as time progresses, more vacancies are created, and the average peak temperature increases gradually due to the presence of more vacancies facilitating electron transport via trap-assisted tunneling. The peak temperature reaches a maximum value when the conductive filament is completely formed.

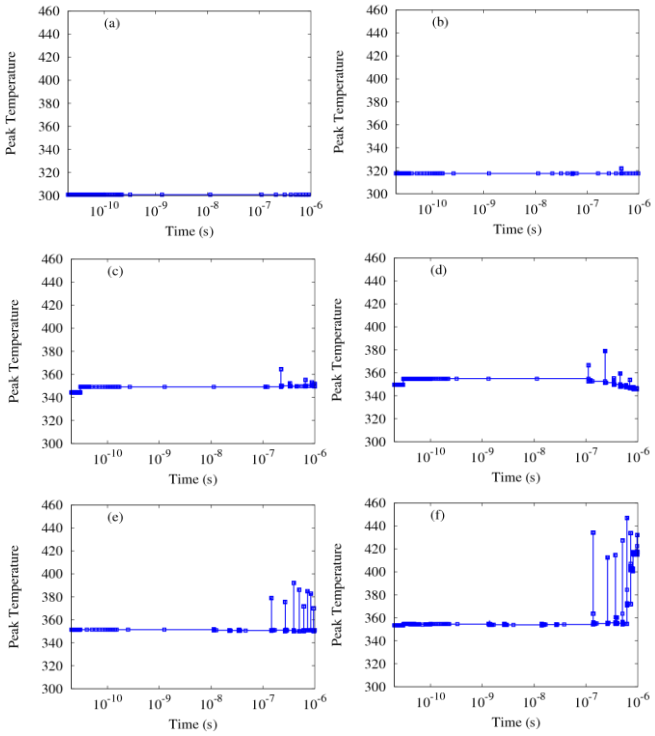

Fig. 8. Variation of the peak temperature with time, as bias is increased (from top to bottom) leading to the creation of the conductive filament.

4.4. Impact of Intrinsic Defects

We compare switching in two different structures: (i) a SiO_2 device having a very low initial concentration of oxygen vacancies and (ii) a SiO_x structure with a Si-rich (high initial concentration) volume. Figs. 9 and 10 show the vacancy distributions for both structures, as the applied bias voltage is ramped up and the conductive filament is formed. For the SiO_2 structure, very few ion-vacancy pairs are created when a low bias is applied (e.g. 0.2V). As we increase the applied bias, more vacancies are created, resulting in the appearance of filament seeds (e.g. 6V). These filament seeds grow visibly when increasing the bias, and at ~7V, an accelerated generation of vacancies takes place, resulting in the formation of a complete CF, which bridges both device contacts. The same process occurs for the Si-rich structure, but the filament creation occurs at lower biases. This is because (as explained in section 3.1) as neutral oxygen vacancies occupied by two electrons result in lowering the activation energy for ion-vacancy generation E_a, defect-rich areas (e.g. in the form of perpendicular columns – as discussed in Ref. [1]) facilitate the creation of a CF at lower applied biases. For the SiO_2 structure, higher forming biases increase the possibility of hard breakdown and hence irreversible ON/OFF transitions. Figs. 9 and 10 illustrate how conductive filaments are of a three-dimensional nature. This stresses the need for the development and use of three-dimensional simulation models, to study accurately the RRAM switching behaviour.

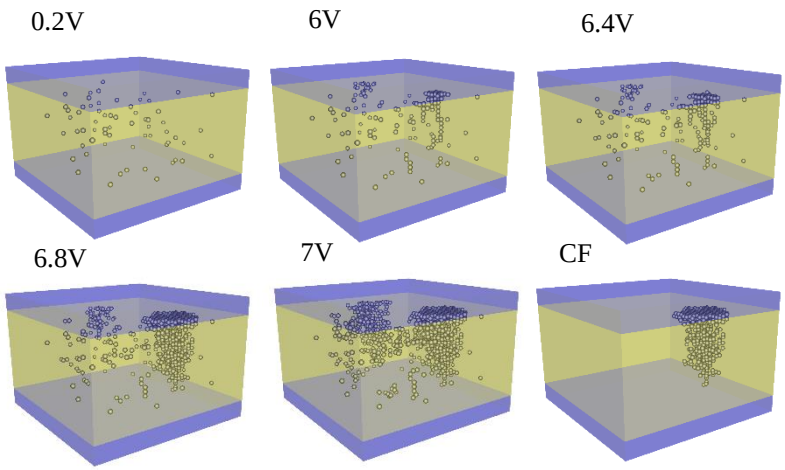

Fig. 9: Vacancy distributions for the pristine ('SiO_2') structure with a low initial concentration of vacancies, as we increase the bias until the CF is formed (~7V). The figure labeled 'CF' illustrates the strongest percolation paths, which are identified using Dijkstra algorithm.

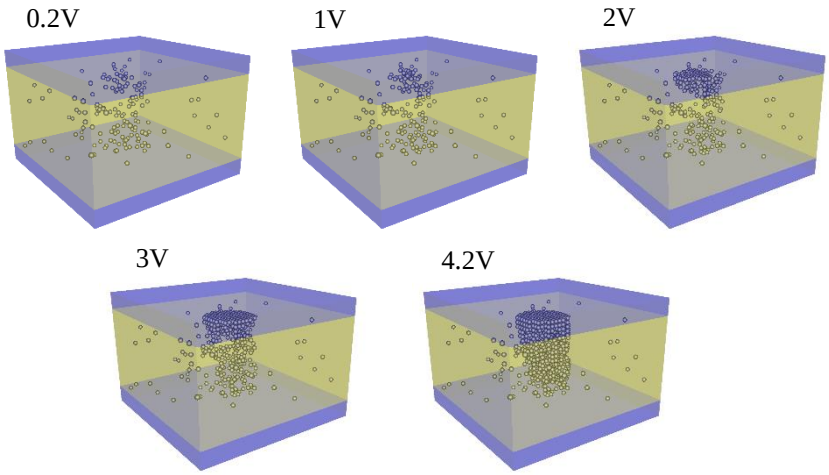

Fig. 10: Vacancy distributions as the bias is ramped up, to create the CF in the silicon-rich silica structure incorporating a defect-rich volume in the form of a column.

5. CONCLUSION

We employed a three-dimensional electrothermal KMC simulator to explore switching in RRAM devices based on silicon-rich silica. The results reinforced the hypothesis that switching is an intrinsic property of the SiO_x layer, as a result of the forming and rupture of conductive filaments in the highly sub-stoichiometric oxide. We demonstrated the important role of self-heating effects and the initial oxygen vacancy distributions acting as precursors for switching. We also discussed the need for three-dimensional physical simulators, and their necessity for a reliable and correct prediction of the switching phenomena. In general, the developed simulator allows us to provide new insight into RRAM device physics, and offers design and optimization capabilities with regard to the reliability and variability of devices and circuits based on resistive memory.

ACKNOWLEDGEMENT

This work is funded by the Engineering and Physical Sciences Research Council (EPSRC–UK) under grant agreement EP/K016776/1.

References

[1] A. Mehonic, S. Cueff, M. Wojdak, S. Hudziak, O. Jambois, C. Labbé, B. Garrido, R. Rizk and A. J. Kenyon, "Resistive switching in silicon sub-oxide films," *J. Appl. Phys.*, vol. 111, pp. 074 507–1–9, April 2012.

[2] L. Chua, "Resistance switching memories are memristors," *Appl. Phys. A*, vol. 102, pp. 765–783, January 2011.

[3] M. Buckwell, L. Montesi, A. Mehonic, O. Reza, L. Garnett, M. Munde, S. Hudziak, and A. J. Kenyon, "Microscopic and spectroscopic analysis of the nature of conductivity changes during resistive switching in silicon-rich silicon oxide," *physica status solidi (c)*, vol. 12, pp. 211–217, January 2015.

[4] A. Mehonic, A. Vrajitoarea, S. Cueff, S. Hudziak, H. Howe, C. Labbe, R. Rizk, M. Pepper, and A. J. Kenyon, "Quantum conductance in silicon oxide resistive memory devices," *Scientific Reports*, vol. 3, pp. 2708–1–7, September 2013.

[5] A. Mehonic, S. Cueff, M. Wojdak, S. Hudziak, C. Labbé, R. Rizk, A. J. Kenyon, "Electrically tailored resistance switching in silicon oxide," *Nanotechnology*, vol. 23, no 45, pp. 455 201–1–9, October 2012.

[6] J. Yao, L. Zhong, D. Natelson and J. M. Tour, "In situ imaging of the conducting filament in a silicon oxide resistive switch," *Nanotechnology*, vol. 2, pp. 242–1–5, January 2012.

[7] A. Chanthbouala, V. Garcia, R. O. Cherifi, K. Bouzehouane, S. Fusil, X. Moya, S. Xavier, H. Yamada, C. Deranlot, N. D. Mathur, M. Bibes, A. Barthélémy, and J. Grollier, "A ferroelectric memristor," *Nat. Mater.*, vol. 11, pp. 860–864, September 2012.

[8] J. Yao, L. Zhong, D. Natelson, and J. M. Tour, "Intrinsic resistive switching and memory effects in silicon oxide," *Applied Physics A*, vol. 102, pp. 835–839, January 2011.

[9] S. Yu, X. Guan, and H.-S. P. Wong, "On the stochastic nature of resistive switching in metal oxide RRAM: Physical modeling, Monte Carlo simulation, and experimental characterization," in *In Electron Devices Meeting (IEDM), 2011 IEEE International*, December 2011, pp. 17.3.1-4.

[10] R. E. Simpson, P. Fons, A. V. Kolobov, T. Fukaya, M. Krbal, T. Yagi, and J. Tominaga, "Interfacial phase-change memory," *Nature Nanotechnology*, vol. 6, pp. 501–505, July 2011.

[11] J. Yao, Z. Sun, L. Zhong, D. Natelson, and J. M. Tour, "Resistive switches and memories from silicon oxide," *Nano Lett.*, vol. 10, pp. 4105–4110, August 2010.

[12] "The ITRS 2010 report," http://http://www.itrs.net/.

[13] D. B. Strukov, G. S. Snider, D. R. Stewart, and R. S. Williams, "The missing memristor found," *Nature*, vol. 453, pp. 80–83, March 2008.

[14] S. C. Chae, J. S. Lee, S. Kim, S. B. Lee, S. H. Chang, C. Liu, B. Kahng, H. Shin, D.-W. Kim, C. U. Jung, S. Seo, M.-J. Lee, and T. W. Noh, "Random circuit breaker network model for unipolar resistance switching," *Advanced Materials*, vol. 20, pp. 1154–1159, March 2008.

[15] R. Waser and M. Aono, "Nanoionics-based resistive switching memories," Nat. Mater., vol. 6, no 11, pp. 833–840, November 2007.

[16] S. H. Jo, T. Chang, I. Ebong, B. B. Bhadviya, P. Mazumder and W. Lu, "Nanoscale memristor device as synapse in neuromorphic systems," *Nano letters*, vol. 10, no 4, pp. 1297-1301, March 2010.

[17] Y. V. Pershin and M. Di Ventra, "Experimental demonstration of associative memory with memristive neural networks," *Neural Networks*, vol. 23, no. 7, pp. 881-886, September 2010.

[18] A. Mehonic and A. J. Kenyon, "Emulating the electrical activity of the neuron using a silicon oxide RRAM cell," *Frontiers in neuroscience*, vol. 10, no 57, pp. 1-10, February 2016.

[19] L. Chua, "Memristor-the missing circuit element," *IEEE Trans. Circuit Theory*, vol. 18, no 5, pp. 507–519, September 1971.

[20] A. Mehonic and A. J. Kenyon, "Resistive Switching in Oxides. In Defects at Oxide Surfaces," *Springer Series in Surface Sciences*, Springer International Publishing, pp. 401-428, February 2015.

[21] T. Sadi, L. Wang, and A. Asenov, "Multi-Scale Electrothermal Simulation and Modelling of Resistive Random Access Memory Devices," International Workshop on Power and Timing Modeling, Optimization and Simulation (PATMOS), pp. 33–37, September 21-23, 2016, Bremen, Germany.

[22] M. Saremi, "Carrier mobility extraction method in ChGs in the UV light exposure," IET Micro & Nano Letters, vol. 11, no. 11, pp. 762–764, 2016.
[23] M. Saremi, H. J. Barnaby, A. Edwards and M. N. Kozicki, "Analytical Relationship between Anion Formation and Carrier-Trap Statistics in Chalcogenide Glass Films," *ECS Electrochemistry Letters*, vol. 4, no 7, pp. H29–H31, 2015.
[24] M. Buckwell, L. Montesi, S. Hudziak, A. Mehonic, A. J. Kenyon. "Conductance tomography of conductive filaments in intrinsic silicon-rich silica RRAM," *Nanoscale*, vol. 7, no 43, pp. 18030-18035, November 2015.
[25] S. Brivio and S. Spiga, "Stochastic circuit breaker network model for bipolar resistance switching memories," *Journal of Computational Electronics*, vol. 16, no. 4, pp. 1154–1166, December 2017.
[26] S. Kim, S.-J. Kim, K. M. Kim, S. R. Lee, M. Chang, E. Cho, Y.-B. Kim, C. J. Kim, U. -I. Chung, and I.-K. Yoo, "Physical electro-thermal model of resistive switching in bi-layered resistance-change memory," *Scientific Reports*, vol. 3, Article number 1680, pp. 1-6, April 2013.
[27] S. Li, W. Chen, Y. Luo, J. Hu, P. Gao, J. Ye, K. Kang, H. Chen, E. Li, and W.-Y. Yin, "Fully Coupled Multiphysics Simulation of Crosstalk Effect in Bipolar Resistive Random Access Memory," *IEEE Trans. Electron Devices*, vol. 64, no. 9, pp. 3647–3653, Sept. 2017
[28] D. Ielmini and V. Milo, "Physics-based modeling approaches of resistive switching devices for memory and in-memory computing applications," *Journal of Computational Electronics*, vol. 16, no 4, pp. 1121–1143, November 2017.
[29] M. A. Villena, J. B. Roldán, F. Jiménez-Molinos, E. Miranda, J. Suñé, M. Lanza, "SIM^2 RRAM: a physical model for RRAM devices simulation," *Journal of Computational Electronics*, vol. 16, no 4, pp 1095–1120, December 2017
[30] Z. Wei and K. Eriguchi, "Analytic Modeling for Nanoscale Resistive Filament Variation in ReRAM With Stochastic Differential Equation," *IEEE Trans. Electron Devices*, vol. 64, no. 5, pp. 2201 – 2206, May 2017.
[31] A. Mehonic, T. Gerard, and A. J. Kenyon, "Light-activated resistance switching in SiO*x* RRAM devices," *Appl. Phys. Lett.*, vol. 111, p. 233502, 2017.
[32] T. Sadi, L. Wang, D. Gao, A. Mehonic, L. Montesi, M. Buckwell, A. Kenyon, A. Shluger, and A. Asenov, "Advanced Physical Modeling of SiO*x* Resistive Random Access Memories," In Proc. Simulation of Semiconductor Processes and Devices (SISPAD), pp. 149–152, September 6-8, 2016, Nuremberg, Germany
[33] G. C. Jegert, "Modeling of Leakage Currents in High-k Dielectrics," Ph.D. Dissertation, Tech. Univ. Munich, Germany, December 2011.
[34] L. Vandelli, A. Padovani, L. Larcher, R. G. Southwick, III, W. B. Knowlton, and G. Bersuker, "A Physical Model of the Temperature Dependence of the Current Through SiO_2/HfO_2 Stacks," *IEEE Trans. Electron Devices*, vol. 58, no. 9, pp. 2878–2887, September 2011.
[35] A. Mehonic, M. Buckwell, L. Montesi, L. Garnett, S. Hudziak, S. Fearn, R. Chater, D. McPhail, and A. J. Kenyon, "Structural changes and conductance thresholds in metal-free intrinsic SiO_x resistive random access memory," *J. Appl. Phys.*, vol. 117, pp. 124505-1-8, March 2015.
[36] J. McPherson, J-Y. Kim, A. Shanware, and H. Mogul, "Thermochemical description of dielectric breakdown in high dielectric constant materials," Appl. Phys. Lett. vol. 82, pp. 2121-2123, March 2003.
[37] A. Mehonic, M. Buckwell, L. Montesi, M. S. Munde, D. Gao, S. Hudziak, R. J. Chater, S. Fearn, D. McPhail, M. Bosman, A. L. Shluger, and A. J. Kenyon. "Nanoscale Transformations in Metastable, Amorphous, Silicon-Rich Silica," *Advanced Materials*, vol. 28, 7486–7493, June 2016.
[38] P. Huang, X.Y. Liu, W.H. Li, Y.X. Deng, B. Chen, Y. Lu, B. Gao, L. Zeng, K.L. Wei, G. Du, X. Zhang, and J.F. Kang, "A Physical Based Analytic Model of RRAM Operation for Circuit Simulation," in *In Electron Devices Meeting (IEDM), 2011 IEEE International*, December 2012, pp. 26.6.1-4.
[39] A. Makarov, V. Sverdlov and S. Selberherr, "Stochastic model of the resistive switching mechanism in bipolar resistive random access memory: Monte Carlo simulations," *Journal of Vacuum Science & Technology B, Nanotechnology and Microelectronics: Materials, Processing, Measurement, and Phenomena*, vol. 29, no. 1, pp. 01AD03-1-5, January 2011.
[40] S. N. Mozaffari, S. Tragoudas, and T. Haniotakis, "More Efficient Testing of Metal-Oxide Memristor–Based Memory," *IEEE Transactions on Computer-Aided Design of Integrated Circuits and Systems*, vol. 36, no. 6, pp. 1018–1029, June 2017.